Journal of Applied Physics

RESEARCH ARTICLE | NOVEMBER 03 2022

Excellent tensile properties and deformation mechanisms in a FeCoNi-based medium entropy alloy with dual-heterogeneous structures

Wenqiang Cheng; Guohao Qin; Muxin Yang; ... et. al

Journal of Applied Physics 132, 175111 (2022)
https://doi.org/10.1063/5.0118217

AIP Publishing

Journal of Applied Physics ARTICLE scitation.org/journal/jap

Excellent tensile properties and deformation mechanisms in a FeCoNi-based medium entropy alloy with dual-heterogeneous structures

Cite as: J. Appl. Phys. **132**, 175111 (2022); doi: 10.1063/5.0118217
Submitted: 4 August 2022 · Accepted: 8 October 2022 ·
Published Online: 3 November 2022

Wenqiang Cheng,[1,2] Guohao Qin,[1,2] Muxin Yang,[1] Wei Wang,[1,a)] and Fuping Yuan[1,2]

AFFILIATIONS

[1]State Key Laboratory of Nonlinear Mechanics, Institute of Mechanics, Chinese Academy of Sciences, No. 15, North 4th Ring, West Road, Beijing 100190, China
[2]School of Engineering Sciences, University of Chinese Academy of Sciences, 19A Yuquan Road, Beijing 100049, China

Note: This paper is part of the Special Topic on Multi-Principal Element Materials: Structure, Property, and Processing.
[a)]**Author to whom correspondence should be addressed:** wangwei2@imech.ac.cn

ABSTRACT

A dual-heterogeneous structure with both heterogeneous grain structure and coherent $L1_2$ nano-precipitate was obtained in a $(FeCoNi)_{86}Al_7Ti_7$ medium-entropy alloy (MEA) after cold rolling, critical annealing, and aging treatments. The volume fraction of the $L1_2$ phase is found to increase from 0% to 34.5% after aging treatment, resulting in severer heterogeneity. The unaged samples of $(FeCoNi)_{86}Al_7Ti_7$ MEA are found to have a much better synergy of strength and ductility as compared to the FeCoNi MEA. Moreover, the tensile properties for the aged samples of $(FeCoNi)_{86}Al_7Ti_7$ MEA with dual-heterogeneous structures are even better than those for the corresponding unaged samples. The hetero-deformation-induced hardening plays a more important role in the aged samples than in the unaged samples, producing a higher density of geometrically necessary dislocations. High density dislocations are discovered in grain interiors for the aged samples and the deformation is dominated by the planar slip in the unaged samples. Meanwhile, a high density of dislocations are observed inside $L1_2$ nano-precipitates; thus, $L1_2$ nano-precipitates can be sheared by dislocations, indicating that $L1_2$ nano-precipitates are strong but deformable. The strong interactions between dislocations and $L1_2$ nano-precipitates should provide additional strain hardening for better tensile properties in the aged samples.

I. INTRODUCTION

High-performance metals and alloys with both high strength and large ductility are always desirable for industrial applications due to the enhanced reliability,[1–9] while it is a big challenge to improve strength and ductility simultaneously in metals and alloys since they are mutually exclusive in general.[2,10,11] Single-phase face-centered cubic (FCC) high-entropy alloys (HEAs)[12–15] and medium-entropy alloys (MEAs),[16–23] consisting of multiple principal elements with nearly equal atomic ratio, have emerged as a promising class of materials in the last two decades due to their superior ductility and toughness at both room and cryogenic temperatures.[15,18,22]

Single-phase FCC HEAs or MEAs with coarse grains have excellent ductility but relatively low yield strength, limiting their engineering applications.[15,18,19] Metals with nanocrystalline grains or ultrafine grains by severe plastic deformation can have gigapascal yield strength, while the tensile ductility is inevitably sacrificed in such homogeneous nanostructures due to the reduced strain hardening.[24,25] This strength-ductility dilemma can be resolved by deploying heterogeneous structures, such as heterogeneous lamellar structure,[26] heterogeneous grain structure,[27–31] gradient structure,[32–38] and dual-phase structure.[1–3,39] The extra hetero-deformation-induced (HDI) hardening can be induced in such heterogeneous structures due to the strain gradients and geometrically necessary dislocations (GNDs) occurred at various domain boundaries.[26,40,41] The deformation incompatibility and stress/strain partitioning among various domains were found to play a vital role in achieving excellent synergy of strength and ductility in such heterogeneous structures.[26]

Precipitates with atomically ordered structures provide an efficient approach for elevating strength. The high density of precipitates can enhance the yield strength to gigapascal level while leading to a reduced resistance to failure, especially when the size of precipitates is large and the phase boundary is non-coherent.[6,7] Nanoprecipitates with coherent boundaries have been proven to be an effective strategy to achieve both high strength and large ductility and evade the strength-ductility tradeoff.[1–3] This strategy has been applied to HEAs and MEAs, and superior tensile properties can be achieved in such nano-precipitated HEAs and MEAs due to the bow-out or cutting precipitation hardening mechanisms.[1–3]

Even better tensile properties might be obtained by deploying coherent nano-precipitates and heterogeneous grain structures at the same time in HEAs or MEAs due to the coupled benefits. In this regard, the dual-heterogeneous structure (both coherent nano-precipitates and heterogeneous grain structure) has been designed and fabricated in a FeCoNi-based MEA [$(FeCoNi)_{86}Al_7Ti_7$], and the tensile properties and the deformation mechanisms for the FeCoNi-based MEA with dual-heterogeneous structure have been investigated and compared with those for a single-phase FCC FeCoNi MEA and for the FeCoNi-based MEA with a single-heterogeneous structure.

II. MATERIALS AND EXPERIMENTAL TECHNIQUES

The FeCoNi MEA ($Fe_{35.8}Co_{32.1}Ni_{32.1}$, in at. %) and the FeCoNi-based MEA ($Fe_{28.8}Co_{28.9}Ni_{28.5}Al_{7.0}Ti_{6.8}$, in at. %) were fabricated by electromagnetic levitation with protection by high-purity argon atmosphere, and all ingots were repeatedly melted for five times to ensure the chemical homogeneity. The materials were homogenized at 1200 °C for 24h followed by water quenching and then hot-forged into plates with a thickness of 9 mm at a starting temperature of 1200 °C and an ending temperature of 1100 °C. The hot-forged plates were annealed at 1150 °C for 2h followed by water quenching and then cold-rolled with a total thickness reduction of about 87%. The cold-rolled FeCoNi samples were annealed at varying temperatures (500–900 °C) for 1.5 min followed by water quenching to obtain various microstructures. For the FeCoNi-based MEA, the samples were first annealed at various temperatures (950–1100 °C) for 1.5 min followed by water quenching to obtain heterogeneous grain structures (these samples are called as unaged samples), and then these annealed samples were aged at 780 °C for 2h to obtain dual-heterogeneous structures (these samples are called as aged samples with a high density of coherent nano-precipitates).

In the quasi-static tensile testing and load–unload–reload testing, specimens with the plated dog-bone shape and gauge section dimensions of $18 \times 2.5 \times 1\ mm^3$ were utilized, and the rolling direction was set to be parallel to the tensile direction. In these tests, an extensometer was used to control and measure the displacement, and the strain rate was set to be 5×10^{-4}/s and the tests were conducted at room temperature. Three tests were conducted for each sample to check the repeatability for tensile properties.

Electron backscattered diffraction (EBSD), x-ray diffraction (XRD), transmission electron microscopy (TEM), high-resolution transmission electron microscopy (HRTEM), and energy disperse spectroscopy (EDS) were used to reveal the microstructures prior to and after tensile testing. The detailed procedures for the sample preparations and the other details of EBSD, TEM, and HRTEM can be found in previous papers.[42] The minimum scanning step for EBSD observation was chosen to be 25 nm, and grain boundaries were only identified by misorientations larger than 15°. Grain reference orientation deviation (GROD) in EBSD was used to distinguish recrystallized grains and calculate recrystallized fraction,[20] the value of GROD less than 2° is defined to distinguish the recrystallized area. The recrystallized fraction is measured based on wide field images with more than 5000 grains.

III. RESULTS AND DISCUSSION

A. Microstructure characterizations prior to tensile testing

In order to identify the phase constitution of the FeCoNi-based MEA with different heat treatments prior to tensile testing, XRD patterns containing the unaged samples (unaged_970 and unaged_1100) and the aged samples (aged_970 and aged_1100) are shown in Fig. 1(a). Since the $L1_2$ precipitate phase is coherent with the FCC matrix phase for the aged samples, each of the diffraction peak is actually an overlap of those two phases. Specifically, in the present work, the (200) fundamental peaks are used to differentiate the contributions of the FCC and $L1_2$ phases. The close-up view of the overlapped (200) asymmetric peak of the FCC phase and the $L1_2$ phase for the aged samples are shown in Fig. 1(b), which indicate the existence of the FCC phase and the $L1_2$ phase. The peak fitting using the Gauss function has been applied to the curve. Then, the relative volume fraction of the $L1_2$ phase in the FCC matrix is calculated based on the integrated peak intensity.[43] Thus, the volume fraction of the $L1_2$ phase is estimated to be about 34.5% and 44.1% for the aged_970 sample and the aged_1100 sample, respectively. XRD patterns also display the presence of the body-centered cubic (BCC) phase but the volume fraction of the BCC phase is very small (<1%).

EBSD observations for selected samples prior to tensile testing are shown in Fig. 2. The inverse pole figures (IPFs) for the unaged_970 and aged_970 samples are shown in Figs. 2(a) and 2(b), respectively, only recrystallized grains are displayed. It is clearly shown that the unaged_970 and aged_970 samples have heterogeneous grain structures consisting of unrecrystallized grains (blacking out area), recrystallized ultrafine grains, and recrystallized coarse grains. The volume fractions of recrystallized grains of the unaged_970 and aged_970 samples are about 57% and 52%, respectively. The distributions of grain sizes of the recrystallized area in the unaged_970 and aged_970 samples are shown in Fig. 2(c), which reveals that the average grain sizes of ultrafine grains are about 0.25 and 0.27 μm, respectively, the average grain sizes of coarse grains are about 2.68 and 2.10 μm, respectively, and the overall average grain sizes are about 0.41 and 0.55 μm, respectively. The IPFs for the unaged_1100 and aged_1100 samples are shown in Figs. 2(d) and 2(e), respectively, in which both samples display homogeneous grain structures with fully recrystallized grains. The distributions of grain sizes of the unaged_1100 and aged_1100 samples are shown in Fig. 2(f), and the average grain sizes are

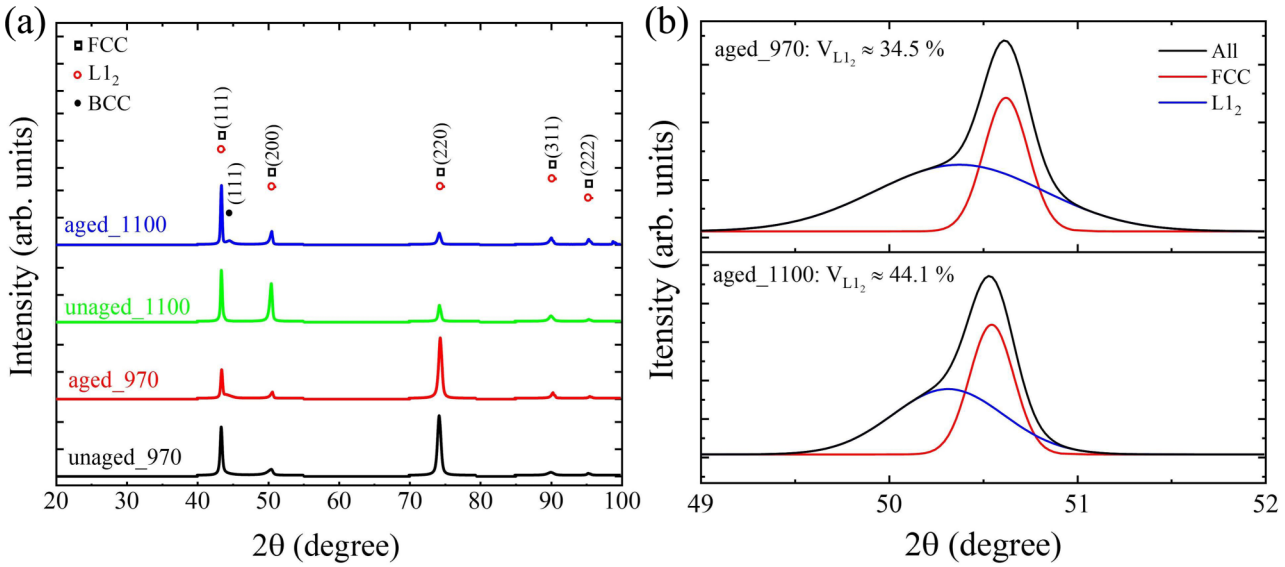

FIG. 1. The measurements of phase constitution of the FeCoNi-based MEA with different heat treatments prior to tensile testing. (a) XRD patterns of the unaged_970, unaged_1100, aged_970, and aged_1100 samples. (b) The close-up view of the overlapped (200) asymmetric peak for the aged samples.

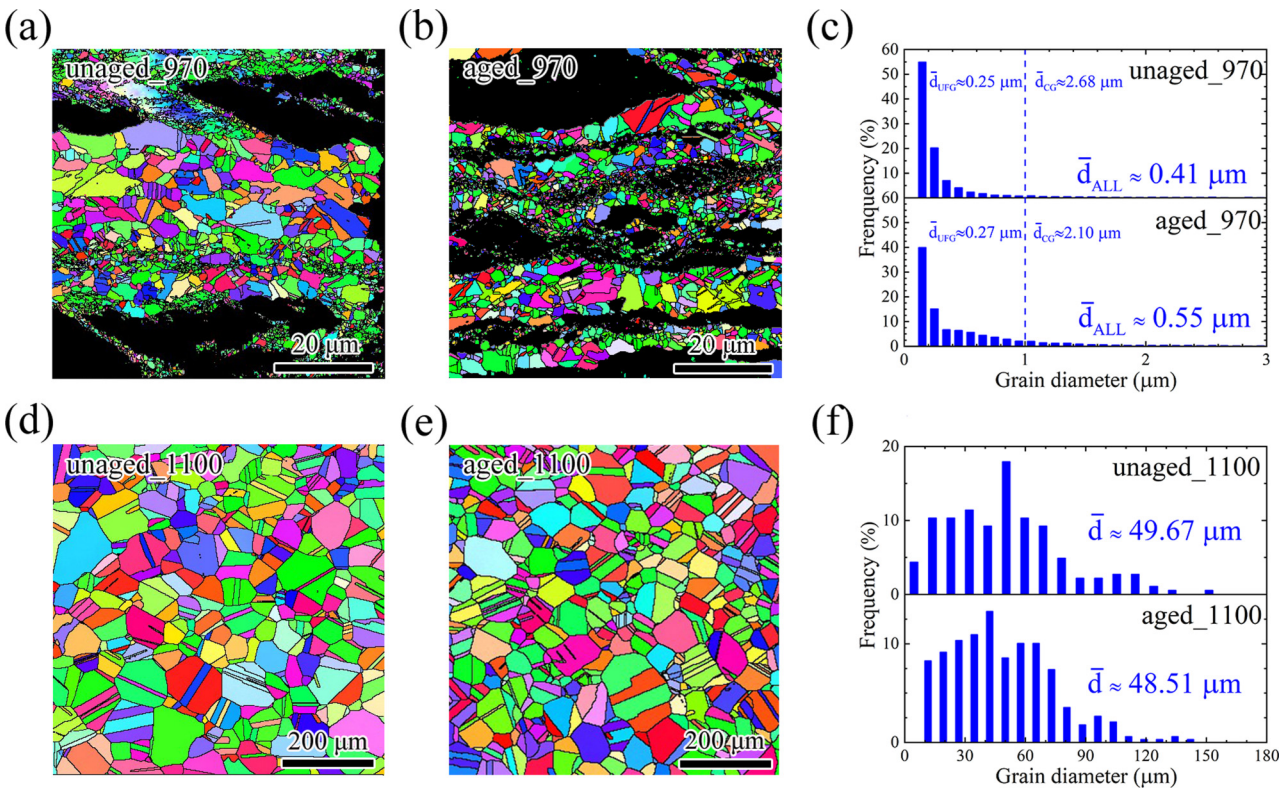

FIG. 2. EBSD observations for selected samples prior to tensile testing. (a) and (b) The IPFs for the unaged_970 and aged_970 samples, respectively. (c) The distributions of grain sizes for the unaged_970 and aged_970 samples. (d) and (e) The IPFs for the unaged_1100 and aged_1100 samples, respectively. (f) The distributions of grain sizes for the unaged_1100 and aged_1100 samples. UFG: ultrafine grain, CG: coarse grain.

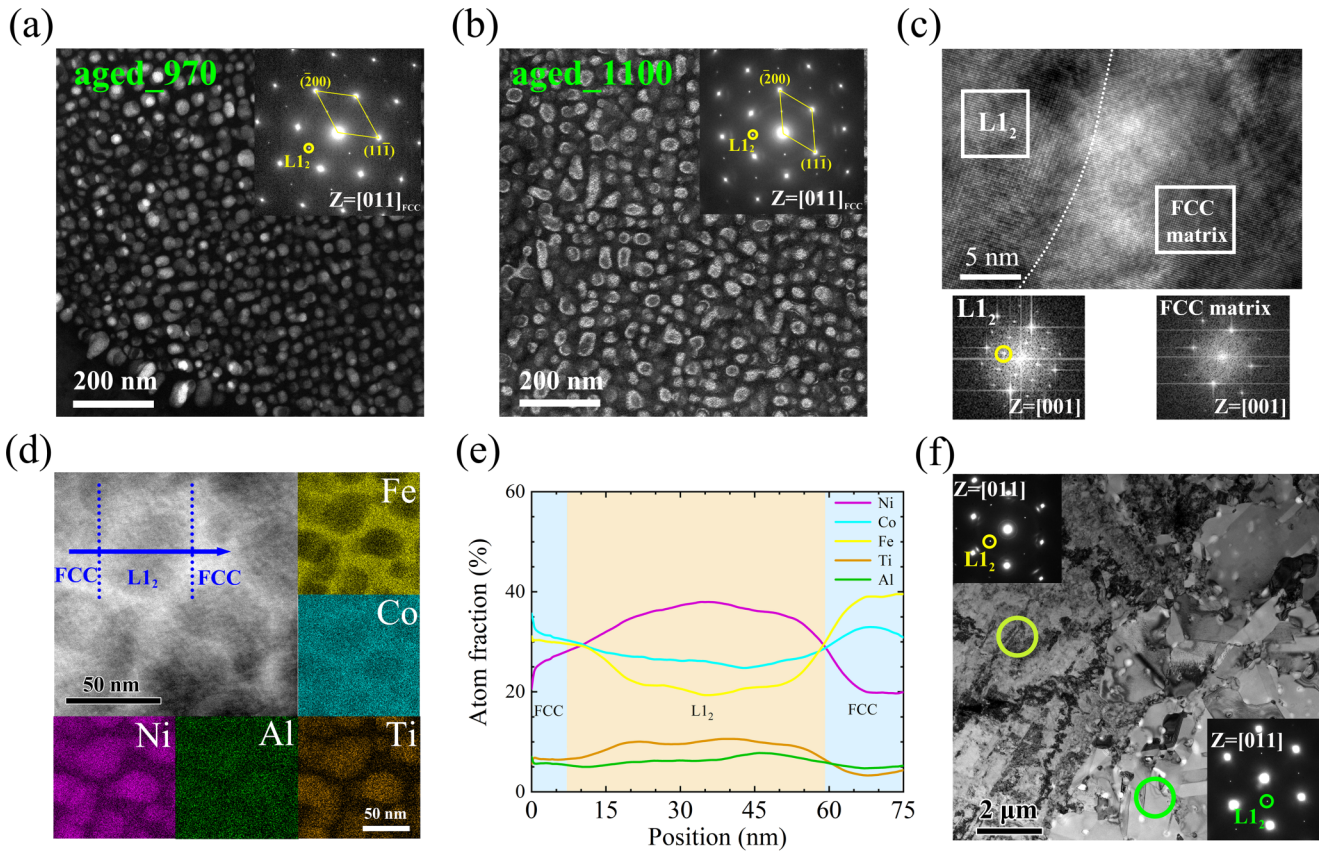

FIG. 3. TEM observations for the aged_970 and aged_1100 samples prior to tensile testing. (a) and (b) Dark-field TEM images for the aged_970 and aged_1100 samples, respectively. (c) The representative high-resolution TEM image for the aged_1100 sample, and the corresponding images after FFT for two marked rectangular areas. (d) The EDS mapping for the aged_1100 sample. (e) Element distributions along the marked line in (d). (f) Bright-field TEM image for the aged_970 sample. The insets show the corresponding SAED patterns for deformed regions (yellow circle) and recrystallized regions (green circle).

about 49.67 and 48.51 μm, respectively. Therefore, the aging treatment has little effect on the FCC matrix.

TEM observations for the aged_970 sample and the aged_1100 sample prior to tensile testing are shown in Figs. 3(a) and 3(b), and the insets show the corresponding selected-area electron diffraction (SAED) patterns. Massive near-spherical $L1_2$ nanoprecipitates (brighter particles) are uniformly distributed within the FCC matrix for both samples. The volume fractions of the $L1_2$ phase are estimated to be about 37.2% and 44.8% based on TEM images for these two samples, and these observations are consistent with the results for XRD measurements. Figure 3(c) shows the representative high-resolution TEM image containing the phase interface between the FCC matrix and the $L1_2$ precipitate, and corresponding images after fast Fourier transformation (FFT) for two marked rectangular areas. The EDS mapping for several $L1_2$ precipitates within a matrix grain is shown in Fig. 3(d). Element distributions along the marked line in Fig. 3(d) are also displayed in Fig. 3(e). Ni, Al, and Ti elements are enriched in the $L1_2$ precipitates, while Fe and Co elements are deprived in the $L1_2$ precipitates. Figure 3(f) shows the TEM observation for the aged_970 sample with partial recrystallization, and the $L1_2$ precipitates are existing in both deformed and recrystallized regions.

B. Outstanding tensile properties

Tensile properties for the FeCoNi MEA, the unaged FeCoNi-based MEA, and the aged FeCoNi-based MEA are displayed in Figs. 4(a)–4(c), respectively, and corresponding plots of yield strength vs uniform elongation are shown in Fig. 4(d). It is clearly shown that the tensile properties of the FeCoNi-based MEA are much better than the FeCoNi MEA, and it is also interesting to note that yield strength and uniform elongation are simultaneously improved after the aging treatment for the FeCoNi-based MEA. Thus, the aged samples display a better synergy of strength and ductility than the unaged samples for the FeCoNi-based MEA. The yield strengths of the various aged samples have elevations of 140–500 MPa compared to the corresponding unaged samples. The strain hardening rate is plotted as a function of true strain for

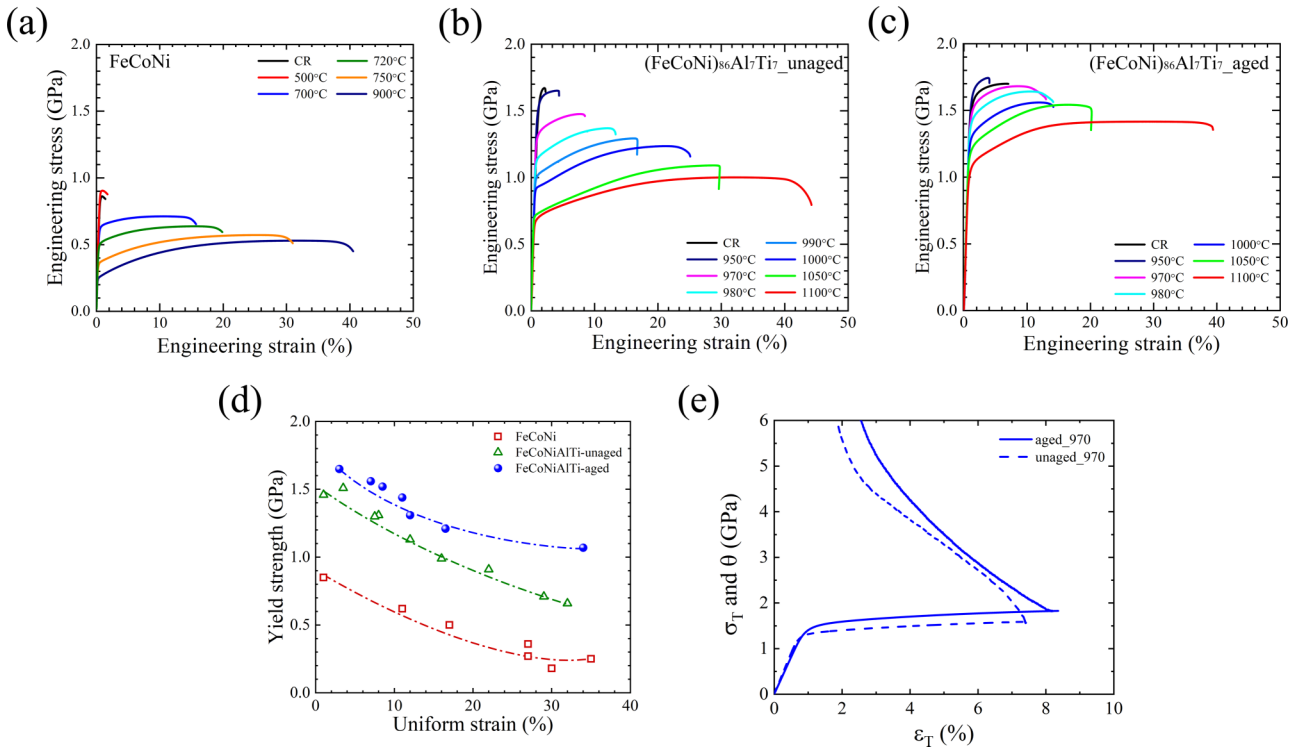

FIG. 4. Tensile properties for various samples. (a)–(c) Engineering stress–strain curves for the FeCoNi MEA, the unaged FeCoNi-based MEA, and the aged FeCoNi-based MEA, respectively. CR: The cold-rolled sample. (d) Yield strength vs uniform elongation for all samples. (e) Strain hardening rate as a function of true strain for selected samples.

selected samples in Fig. 4(e). The strain hardening rate is discovered to be higher for the aged samples as compared to the corresponding unaged samples, indicating a stronger strain hardening after the aging treatment.

C. Hetero-deformation-induced hardening

According to previous research,[20,26,27,40,41] HDI hardening plays an important role in the plastic deformation stage for the heterogeneous structure due to various domains with dramatically different strengths or hardnesses, resulting in an additional strain hardening capacity and better tensile properties. Thus, the observed higher hardening rate for the aged samples can be attributed to the severer heterogeneity after the aging treatment. Load–unload–reload tensile tests were conducted to unveil the HDI hardening effect and the underlying strain hardening mechanism. Load–unload–reload curves for the unaged_970 and aged_970 samples are displayed in Fig. 5(a). Each load–unload–reload curve has several hysteresis loops. The close-up view of typical hysteresis loops under a selected unloading strain is shown in Fig. 5(b). The larger the loop width, the stronger the HDI hardening.[20,26,44] The aged_970 sample displays larger loop width due to the heterogeneous grain structure and the coherent precipitate phase, resulting in larger HDI stress. The calculation method for HDI stress can be seen from our previous paper.[40] Figure 5(c) shows the HDI stress as a function of true strain, the value of the aged_970 sample is larger than the unaged_970 sample, and the result is consistent with the corresponding loop widths as shown in Fig. 5(b). These observations indicate that the aged samples display a higher HDI hardening than the unaged samples, resulting in better tensile properties.

D. Microstructure characterizations after tensile testing

In general, GNDs induced from strain gradients between hard and soft domains provide HDI hardening.[20,26,40,41,45] The density of GNDs can be estimated by the kernel average misorientation (KAM) value using a method based on the strain gradient theory, which was proposed by Gao and Kubin,[46,47]

$$\rho_{GND} = 2\theta/lb, \tag{1}$$

where ρ_{GND} is the GND density at local points, θ is the misorientation at local points, l is the unit length for the local points, and b is Burger's vector for the materials. The GND mappings prior to and after tensile testing for the unaged_970 and aged_970 samples have been characterized by EBSD and are displayed in Fig. 6.

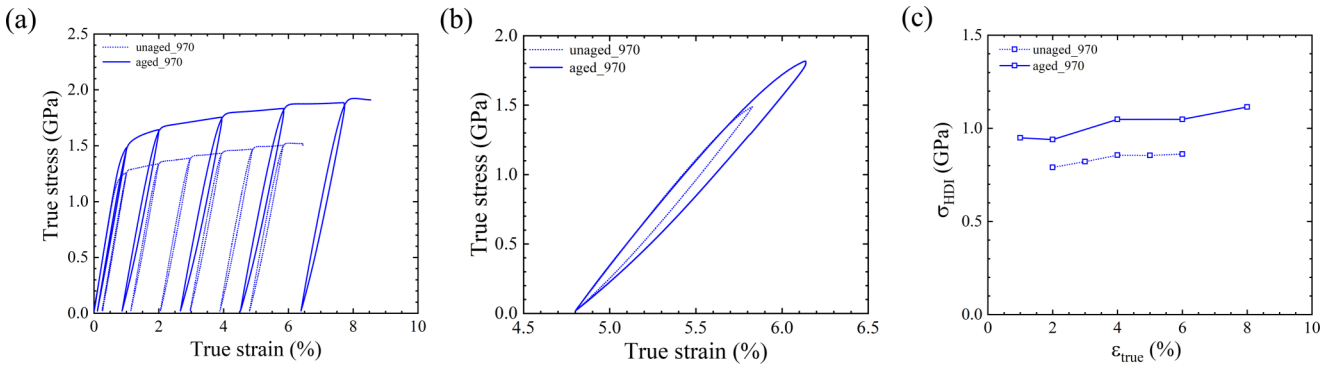

FIG. 5. HDI hardening for the unaged_970 and aged_970 samples. (a) Load–unload–reload curves. (b) Close-up view of typical hysteresis loops. (c) HDI stress as a function of true strain.

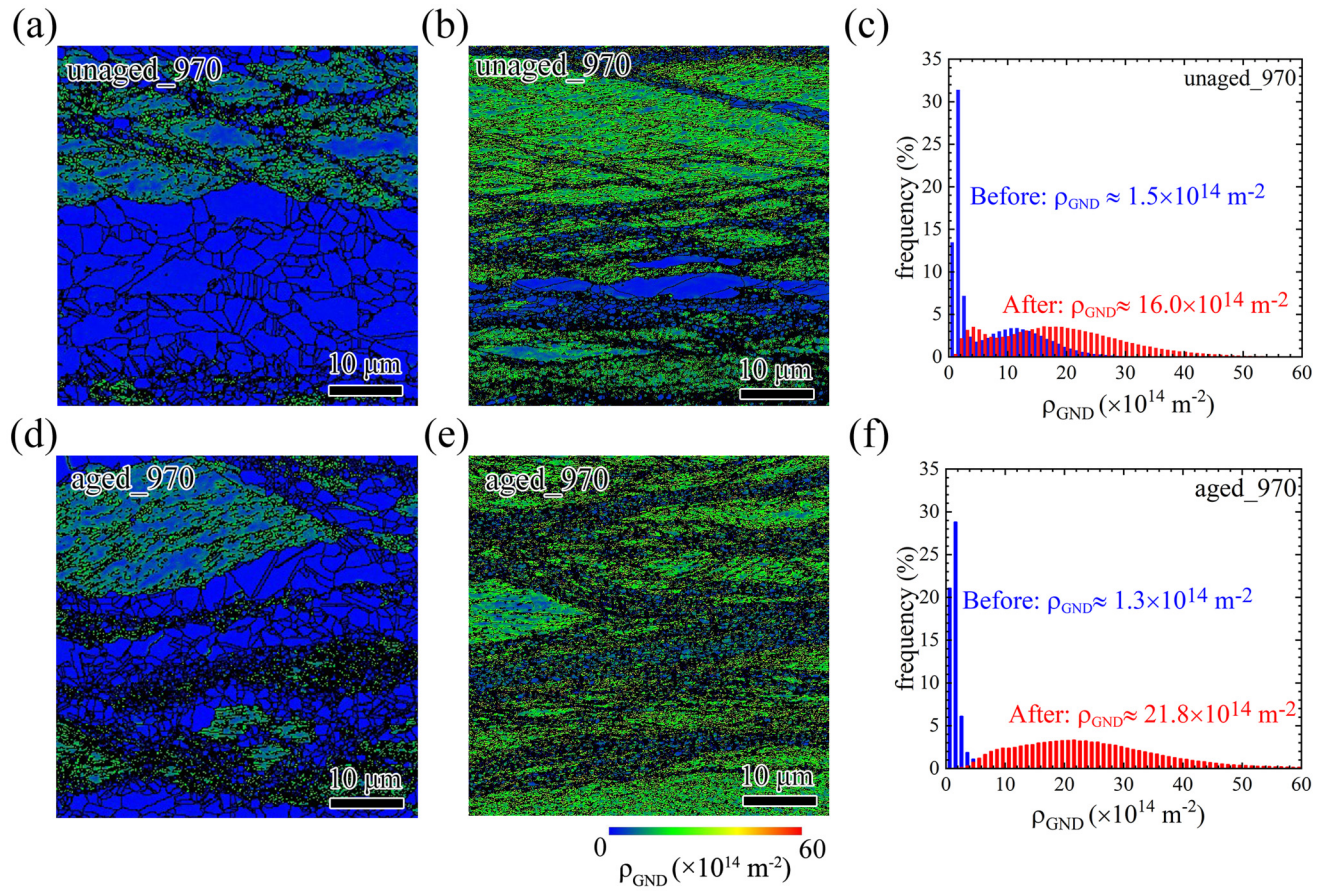

FIG. 6. (a) and (b) GND mappings for the unaged_970 sample prior to and after tensile testing, respectively. (c) The histogram distribution of the GND value prior to and after tensile testing for the unaged_970 sample. (d) and (e) GND mappings for the aged_970 sample prior to and after tensile testing, respectively. (f) The histogram distribution of the GND value prior to and after tensile testing for the aged_970 sample.

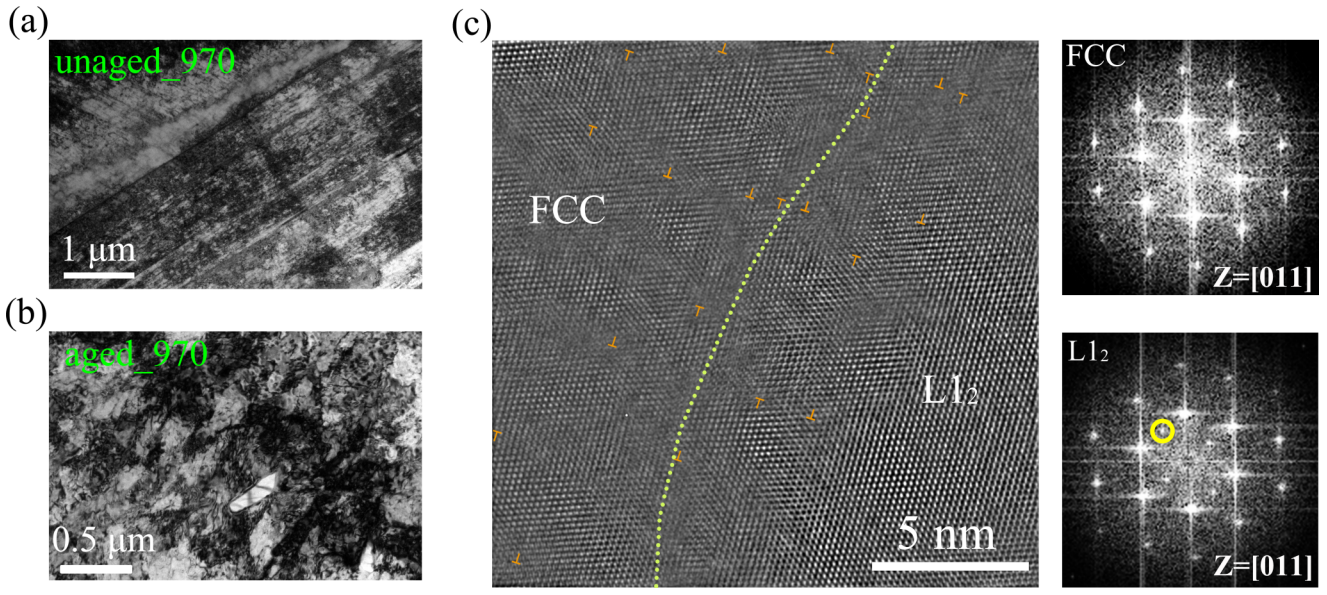

FIG. 7. TEM observations after tensile testing for the unaged_970 and aged_970 samples. (a) The unaged_970 sample. (b) The aged_970 sample. (c) HRTEM image for the aged_970 sample, in which the insets show the corresponding images after FFT for FCC matrix and $L1_2$ phase.

Figures 6(a) and 6(b) show the GND mappings for the unaged_970 sample prior to and after tensile testing, respectively. Figures 6(d) and 6(e) show the GND mappings for the aged_970 sample prior to and after tensile testing, respectively. Then, the histogram distributions of the GND values prior to and after tensile testing for the unaged_970 and aged_970 samples are displayed in Figs. 6(c) and 6(f), respectively. Moreover, the average GND values prior to and after tensile testing for these two samples are also calculated and indicated in Figs. 6(c) and 6(f), respectively. The average GND values prior to tensile testing for these two samples are almost equal. However, the average GND value for the aged_970 sample ($21.8 \times 10^{14}\,m^{-2}$) is larger than that for the unaged_970 sample ($16.0 \times 10^{14}\,m^{-2}$) after tensile testing. In the aged_970 sample, GNDs can be produced at the boundaries of various domains (coarse grains, ultrafine grains, unrecrystallized grains, and $L1_2$ precipitates), which will result in larger HDI hardening for better tensile properties.

The microstructural deformation mechanisms for the unaged_970 and aged_970 samples have been compared and revealed by TEM observations after tensile testing, as shown in Fig. 7. High density dislocations are discovered in grain interiors for the unaged_970 sample and the deformation is dominated by the planar slip of dislocations along the {111} primary slip planes, as shown in Fig. 7(a). Figure 7(b) shows even higher density non-planar dislocations in the aged_970 sample. Moreover, it is clearly shown that dislocations can be found both around $L1_2$ nano-precipitates and inside $L1_2$ nano-precipitates, as shown in Fig. 7(c), indicating that $L1_2$ nano-precipitates can be sheared by dislocations. Thus, $L1_2$ nano-precipitates are strong but deformable. The strong interactions between dislocations and $L1_2$ nano-precipitates should provide additional strain hardening for better tensile properties in the aged samples, which is consistent with Fig. 5(c).

IV. CONCLUSIONS

In summary, the aged FeCoNi-based MEA with dual-heterogeneous structure (both coherent nanoprecipitates and heterogeneous grain structure) is found to have better tensile properties as compared to the corresponding unaged samples.

First, since GNDs can be produced at the boundaries of various domains (coarse grains, ultrafine grains, unrecrystallized grains, and $L1_2$ precipitates) during tensile deformation, the aged samples produce higher HDI hardening than the unaged samples.

Second, the deformation is dominated by planar slip for the unaged samples. Higher density non-planar dislocations are discovered in grain interiors for the aged samples.

Third, $L1_2$ nano-particles can be sheared by dislocations, indicating that the $L1_2$ nano-precipitates are strong but deformable. The strong interactions between dislocations and $L1_2$ nano-precipitates should provide additional strain hardening for better tensile properties in the aged samples.

The present findings should provide insights into the microstructural design to achieve excellent mechanical properties in structural metallic materials.

ACKNOWLEDGMENTS

This research was supported by the National Key R&D Program of China (No. 2017YFA0204402), the NSFC Basic Science Center Program for "Multiscale Problems in Nonlinear Mechanics"

(No. 11988102), and the National Natural Science Foundation of China (NNSFC) (Nos. 11790293 and 52192591).

AUTHOR DECLARATIONS

Conflict of Interest

The authors have no conflicts to disclose.

Author Contributions

Wenqiang Cheng: Data curation (lead); Investigation (lead); Validation (supporting). **Guohao Qin:** Data curation (equal); Investigation (supporting). **Muxin Yang:** Validation (lead). **Wei Wang:** Conceptualization (equal); Writing – original draft (lead); Writing – review & editing (equal). **Fuping Yuan:** Conceptualization (equal); Writing – review & editing (equal).

DATA AVAILABILITY

The data that support the findings of this study are available from the corresponding author upon reasonable request.

REFERENCES

[1]X. H. Du, W. P. Li, H. T. Chang, T. Yang, G. S. Duan, B. L. Wu, J. C. Huang, F. R. Chen, C. T. Liu, W. S. Chuang, Y. Lu, M. L. Sui, and E. W. Huang, Nat. Commun. **11**, 7 (2020).
[2]T. Yang, Y. L. Zhao, Y. Tong, Z. B. Jiao, J. Wei, J. X. Cai, X. D. Han, D. Chen, A. Hu, J. J. Kai, K. Lu, Y. Liu, and C. T. Liu, Science **362**, 933, (2018).
[3]L. Fan, T. Yang, Y. L. Zhao, J. H. Luan, G. Zhou, H. Wang, Z. B. Jiao, and C. T. Liu, Nat. Commun. **11**, 8 (2020).
[4]H. Aydin, E. Essadiqi, I. H. Jung, and S. Yue, Mater. Sci. Eng. A **564**, 501 (2013).
[5]O. Bouaziz, H. Zurob, and M. X. Huang, Steel Res. Int. **84**, 937 (2013).
[6]S. H. Kim, H. Kim, and N. J. Kim, Nature **518**, 77 (2015).
[7]Z. W. Wang, W. J. Lu, H. Zhao, C. H. Liebscher, J. Y. He, D. Ponge, D. Raabe, and Z. M. Li, Sci. Adv. **6**, 7 (2020).
[8]I. Gutierrez-Urrutia and D. Raabe, Acta Mater. **59**, 6449 (2011).
[9]J. H. Choi, M. C. Jo, H. Lee, A. Zargaran, T. Song, S. S. Sohn, N. J. Kim, and S. Lee, Acta Mater. **166**, 246 (2019).
[10]R. O. Ritchie, Nat. Mater. **10**, 817 (2011).
[11]J. Y. He, H. Wang, H. L. Huang, X. D. Xu, M. W. Chen, Y. Wu, X. J. Liu, T. G. Nieh, K. An, and Z. P. Lu, Acta Mater. **102**, 187 (2016).
[12]J. W. Yeh, S. K. Chen, S. J. Lin, J. Y. Gan, T. S. Chin, T. T. Shun, C. H. Tsau, and S. Y. Chang, Adv. Eng. Mater. **6**, 299 (2004).
[13]B. Cantor, I. T. H. Chang, P. Knight, and A. J. B. Vincent, Mater. Sci. Eng. A **375-377**, 213 (2004).
[14]E. P. George, D. Raabe, and R. O. Ritchie, Nat. Rev. Mater. **4**, 515 (2019).
[15]B. Gludovatz, A. Hohenwarter, D. Catoor, E. H. Chang, E. P. George, and R. O. Ritchie, Science **345**, 1153, (2014).
[16]S. S. Sohn, A. K. da Silva, Y. Ikeda, F. Kormann, W. J. Lu, W. S. Choi, B. Gault, D. Ponge, J. Neugebauer, and D. Raabe, Adv. Mater. **31**, 8 (2019).
[17]Z. Wu, H. Bei, G. M. Pharr, and E. P. George, Acta Mater. **81**, 428 (2014).
[18]B. Gludovatz, A. Hohenwarter, K. V. S. Thurston, H. B. Bei, Z. G. Wu, E. P. George, and R. O. Ritchie, Nat. Commun. **7**, 8 (2016).
[19]J. Miao, C. E. Slone, T. M. Smith, C. Niu, H. Bei, M. Ghazisaeidi, G. M. Pharr, and M. J. Mills, Acta Mater. **132**, 35 (2017).
[20]M. X. Yang, D. S. Yan, F. P. Yuan, P. Jiang, E. Ma, and X. L. Wu, Proc. Natl. Acad. Sci. U.S.A. **115**, 7224 (2018).
[21]Y. Ma, F. P. Yuan, M. X. Yang, P. Jiang, E. Ma, and X. L. Wu, Acta Mater. **148**, 407 (2018).
[22]M. X. Yang, L. L. Zhou, C. Wang, P. Jiang, F. P. Yuan, E. V. Ma, and X. L. Wu, Scr. Mater. **172**, 66 (2019).
[23]X. L. Wu, M. X. Yang, P. Jiang, C. Wang, L. L. Zhou, F. P. Yuan, and E. Ma, Scr. Mater. **178**, 452 (2020).
[24]H. Gleiter, Prog. Mater. Sci. **33**, 223 (1989).
[25]Y. T. Zhu and X. Z. Liao, Nat. Mater. **3**, 351 (2004).
[26]X. L. Wu, M. X. Yang, F. P. Yuan, G. L. Wu, Y. J. Wei, X. X. Huang, and Y. T. Zhu, Proc. Natl. Acad. Sci. U.S.A. **112**, 14501 (2015).
[27]X. L. Wu and Y. T. Zhu, Mater. Res. Lett. **5**, 527 (2017).
[28]Y. M. Wang, M. W. Chen, F. H. Zhou, and E. Ma, Nature **419**, 912 (2002).
[29]M. Song, R. Zhou, J. Gu, Z. W. Wang, S. Ni, and Y. Liu, Appl. Mater. Today **18**, 6 (2020).
[30]C. L. Chu, W. P. Chen, J. C. Liu, Q. Chen, and Z. Q. Fu, Rare Met. **41**, 2864 (2022).
[31]F. L. Jiang, C. C. Zhao, D. S. Liang, W. W. Zhu, Y. W. Zhang, S. Pan, and F. Z. Ren, Mater. Sci. Eng. A **771**, 138625 (2020).
[32]T. H. Fang, W. L. Li, N. R. Tao, and K. Lu, Science **331**, 1587, (2011).
[33]X. L. Wu, P. Jiang, L. Chen, F. P. Yuan, and Y. T. T. Zhu, Proc. Natl. Acad. Sci. U.S.A. **111**, 7197 (2014).
[34]K. Lu, Science **345**, 1455, (2014).
[35]X. L. Wu, P. Jiang, L. Chen, J. F. Zhang, F. P. Yuan, and Y. T. Zhu, Mater. Res. Lett. **2**, 185 (2014).
[36]A. Y. Chen, J. B. Liu, H. T. Wang, J. Lu, and Y. M. Wang, Mater. Sci. Eng. A **667**, 179 (2016).
[37]Y. J. Wei, Y. Q. Li, L. C. Zhu, Y. Liu, X. Q. Lei, G. Wang, Y. X. Wu, Z. L. Mi, J. B. Liu, H. T. Wang, and H. J. Gao, Nat. Commun. **5**, 8 (2014).
[38]L. B. Chen, T. H. Cao, R. Wei, K. Tang, C. Xin, F. Jiang, and J. Sun, Mater. Sci. Eng. A **772**, 8 (2020).
[39]F. He, Z. S. Yang, S. F. Liu, D. Chen, W. T. Lin, T. Yang, D. X. Wei, Z. J. Wang, J. C. Wang, and J. J. Kai, Int. J. Plast. **144**, 15 (2021).
[40]M. X. Yang, Y. Pan, F. P. Yuan, Y. T. Zhu, and X. L. Wu, Mater. Res. Lett. **4**, 145 (2016).
[41]Y. T. Zhu and X. L. Wu, Mater. Res. Lett. **7**, 393 (2019).
[42]W. Wang, Y. K. Liu, Z. H. Zhang, M. X. Yang, L. L. Zhou, J. Wang, P. Jiang, F. P. Yuan, and X. L. Wu, J. Mater. Sci. Technol. **132**, 110 (2023).
[43]A. M. Manzoni, S. Haas, J. M. Yu, H. M. Daoud, U. Glatzel, H. Aboulfadl, F. Mucklich, R. Duran, G. Schmitz, D. M. Tobbens, S. Matsumura, F. Vogel, and N. Wanderka, Mater. Charact. **154**, 363 (2019).
[44]C. W. Sinclair, G. Saada, and J. D. Embury, Philos. Mag. **86**, 4081 (2006).
[45]X. L. Wu and Y. T. Zhu, MRS Bull. **46**, 244 (2021).
[46]H. Gao, Y. Huang, W. D. Nix, and J. W. Hutchinson, J. Mech. Phys. Solids **47**, 1239 (1999).
[47]L. P. Kubin and A. Mortensen, Scr. Mater. **48**, 119 (2003).